

LA-UR-08-04000

Approved for public release;
distribution is unlimited.

Title: Known Residual Stress Specimens Using Opposed Indentation

Author(s): P. Pagliaro (U. Palermo)
M. B. Prime (WT-2)
B. Clausen (LANSCE-LC)
M. L. Lovato (MST-8),
B. Zuccarello (U. Palermo)

Details: Journal of Engineering Materials and Technology
Volume 131, 031002 (2009).



Los Alamos National Laboratory, an affirmative action/equal opportunity employer, is operated by the Los Alamos National Security, LLC for the National Nuclear Security Administration of the U.S. Department of Energy under contract DE-AC52-06NA25396. By acceptance of this article, the publisher recognizes that the U.S. Government retains a nonexclusive, royalty-free license to publish or reproduce the published form of this contribution, or to allow others to do so, for U.S. Government purposes. Los Alamos National Laboratory requests that the publisher identify this article as work performed under the auspices of the U.S. Department of Energy. Los Alamos National Laboratory strongly supports academic freedom and a researcher's right to publish; as an institution, however, the Laboratory does not endorse the viewpoint of a publication or guarantee its technical correctness.

Known Residual Stress Specimens Using Opposed Indentation

Pierluigi Pagliaro,^{1,*} Michael B. Prime,^{2,†} Bjørn Clausen,²

Manuel L. Lovato,² and Bernardo Zuccarello¹

¹*Dipartimento di Meccanica, Università degli Studi di Palermo, 90128 Palermo, Italy*

²*Los Alamos National Laboratory, Los Alamos, NM 87544, USA*

(Dated: September 29, 2008)

Abstract

In order to test new theories for residual stress measurement or to test the effects of residual stress on fatigue, fracture and stress corrosion cracking, a known stress test specimen was designed and then fabricated, modeled, and experimentally validated. To provide a unique biaxial stress state, a 60 mm diameter 10 mm thick disk of 316L stainless steel was plastically compressed through the thickness with opposing 15 mm diameter hard steel indenters in the center of the disk. For validation, the stresses in the specimen were first mapped using time-of-flight neutron diffraction and Rietveld full pattern analysis. Next, the hoop stresses were mapped on a cross-section of two disks using the contour method. The contour results were very repeatable and agreed well with the neutron results. The indentation process was modeled using the finite element method. Because of a significant Bauschinger effect, accurate modeling required testing the cyclic behavior of the steel and then modeling it using a Chaboche-type combined hardening law. The model results agreed very well with the measurements. The duplicate contour measurements demonstrated stress repeatability better than 0.01% of the elastic modulus and allowed discussion of implications of measurements of parts with complicated geometries.

Keywords: Residual stress; contour method; neutron diffraction

*Visiting student at the Los Alamos National Laboratory; Electronic address: pagliaro@dima.unipa.it;

URL: <http://www.dima.unipa.it/~pagliaro>

†Electronic address: prime@lanl.gov; URL: <http://public.lanl.gov/prime>

I. INTRODUCTION

Residual stresses play a significant role in many material failure processes like fatigue, fracture, stress corrosion cracking, buckling and distortion¹. Residual stresses are the stresses present in a part free from any external load, and they are generated by virtually any manufacturing process. Because of their important contribution to failure and their almost universal presence, the knowledge of residual stress is crucial for prediction of the strength of any engineering structure. However, the prediction of residual stresses is a very complex problem. In fact, the development of residual stress generally involves nonlinear material behavior, phase transformation, coupled mechanical and thermal problems and/or varying mechanical properties throughout the material. Hence, the ability to accurately quantify residual stresses through measurement is an important engineering tool.

A hypothesized improvement to the contour method that needs experimental validation motivated this study to produce a novel test specimen. In the literature there are many residual stress measurement techniques. Each of them has its advantages and disadvantages, and its own accuracy. The recently developed contour method is one of the few methods that can measure a 2-D map of internal stresses, and it can be applied to many parts that are difficult for other methods²⁻⁸. As originally presented, the contour method only measured the stress component normal to the cross-section of measurement. More recent extensions to the contour method^{9,10} determine multiple components using multiple cuts. However, in theory one should be able to measure multiple components with a single cut if subsequent measurements are taken on the cut surface with other techniques. A test specimen with significant stresses in two directions that were also significantly different from each other would provide the most convincing validation of the new theory. Since both the new theory and the independent validation would require other measurement methods, the specimen would have to be possible to measure with multiple techniques.

Another important use for known stress specimens is to experimentally test the effects of residual stress on fatigue, fracture, creep, stress corrosion cracking, or other material behavior¹¹.

Most common residual stress test specimens are not ideal for the required validation purposes. Various procedure for introducing residual stresses into a test specimen have been used. The most common is a plastically bent beam producing a typical zigzag residual

stress distribution through the thickness^{12,13}. However, a bent beam produces only uniaxial stresses, which are not satisfactory for this validation. Other common validation specimens are based on producing multiple specimens identically with a stress inducing process such as peening and then measuring the stresses with some other technique. A specimen with stresses that could be easily predicted or modeled would provide the additional benefit of not requiring extensive independent measurements.

This paper presents the design, fabrication, the material characterization and the finite element (FE) prediction of the residual stresses of the specimen described in the earlier paragraph. Furthermore, in order to measure the residual stress field produced with this technique, a neutron diffraction experiment was executed on this specimen. Then the contour method was applied to two different test specimens, the specimen and a virtually identical second specimen, and it was possible to verify its good repeatability.

II. SPECIMEN DESIGN

A test specimen was designed to provide a residual stress distribution particularly well suited for a specific experimental validation. It was desired to validate the multiple-component contour method on different stress states where the two significant normal stress components were approximately equal (i.e. equi-biaxial) and, conversely, of opposite sign. Such stress states can be produced in a single shrink-fit ring and plug, in which the expansion of a cooled, oversized plug is constrained by a surrounding ring resulting in biaxial compressive residual stresses in the plug. The ring experiences compressive radial stresses under the forces from the plug, but the hoop stresses are tensile.

Since a real ring and plug would fall apart during contour method cutting, an alternative configuration to produce a similar residual stress distribution was used. A circular disk was plastically compressed through the thickness by two cylindrical indenters of smaller diameter, see Fig. 1(a). A similar specimen was recently used to study fatigue and fracture behavior¹¹. The compressed region between the two indenters yields and wants to expand in the radial direction due to the Poisson effect. Under the constraint of the surrounding material, analogous to the ring in the example of a shrink-fit ring and plug, a biaxial (hoop and radial) compressive residual stress state is produced in the central region, while in the outer region there will be tensile and compressive residual stresses for hoop and radial stresses,

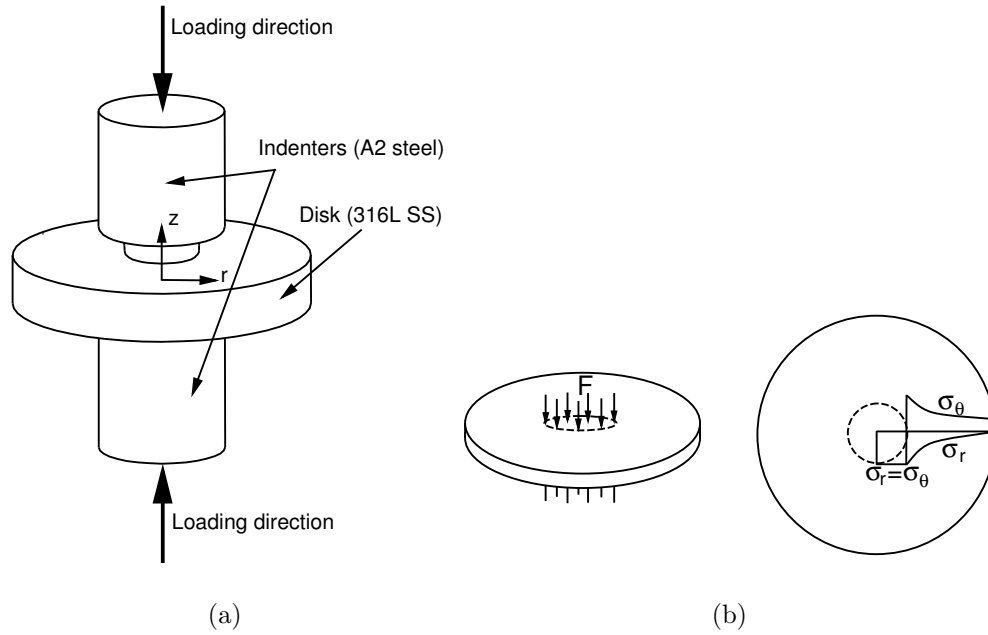


FIG. 1: Schematic diagram illustrating (a) the indentation process, (b) the conceptual residual stress distribution obtained.

respectively (see Fig. 1(b)). Obviously, the real residual stress field will be continuous and not discontinuous like in the shrink-fit ring and plug, because in this case we have only one part.

The geometry of the specimen was then designed considering the material behavior and experimental limitations. A 60 mm diameter 10 mm thick disk was chosen with the indenters 15 mm in diameter, see Fig. 2. The thickness was chosen based on the limited penetration of neutrons through steel. The diameters of the disk and the indenters were chosen to obtain a stress gradients that could be resolved using reasonable neutron sampling volumes, to obtain a relaxed contour of at least $20 \mu\text{m}$ (peak-to-valley) for the contour method measurement and also considering the maximum load of the test machine (100 kN). Furthermore, the shape of the indenters was designed to reduce the stress concentration due to sharp corners. To optimize the design for these considerations, several preliminary finite element simulations of the indentation process were carried out. The indenter material used was an A2 tool steel, characterized by a high hardness (58 HRC) and a high yield stress (about 1300 MPa). The Young modulus of A2 tool is 204 GPa and Poisson's ratio is 0.3. In order to center the two indenters with respect to the disk, two PMMA rings were designed (see Fig. 2), which are moved out of the way prior to indentation.

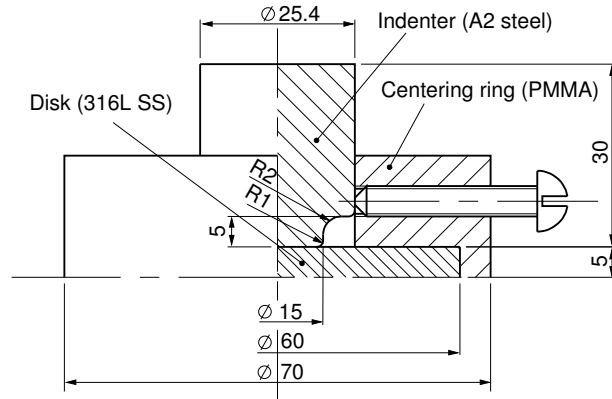


FIG. 2: Quarter-symmetry drawing of the indentation fixture, dimensions in mm. $R1=1$ mm and $R2=3$ mm.

III. MATERIALS

316L stainless steel was chosen for the material as the best compromise among the ideal materials for the different measurement methods that will be required to validate the multiple stress component theories. For the contour method, hole drilling, and other relaxation methods, it is generally better to have a material with high S_y/E in order to obtain more relaxation. In general, the material yield strength, S_y , limits the residual stress magnitudes. An aluminum alloy would be a good choice (S_y/E can easily exceed $4000 \mu\epsilon$), but, unfortunately, it is usually not as good for x-ray diffraction measurements. Austenitic steel has a lower S_y/E ($\approx 950 \mu\epsilon$), which means lower relaxed strains, but it is very good for neutron diffraction and x-ray diffraction. 316L stainless steel was chosen based on previous successful diffraction measurements and industrial importance. The disk was machined from a hot cross-rolled plate (457 mm x 457 mm and 12.7 mm thickness) of 316L stainless steel. The chemical composition of the 316L Stainless steel is in weight percent: C=0.018, Mn=1.59, P=0.031, S=0.005, Si=0.23, Ni=10.64, Cr=16.65, Mo=2.16, N=0.05 and Fe=balance (in accord with the ASTM A240 and ASME SA-240).

To have the residual stress produced only by indentation, the material must be initially stress-free. For this reason, the plate was annealed at 1050 °C for 30 minutes in vacuum and then slow cooled to room temperature in argon in order to remove any preexisting residual stresses. Then, to verify the absence of any preexisting residual stresses, a slitting method test¹⁴ was executed. A square specimen (60 mm x 60 mm x 12.7 mm) was extracted from

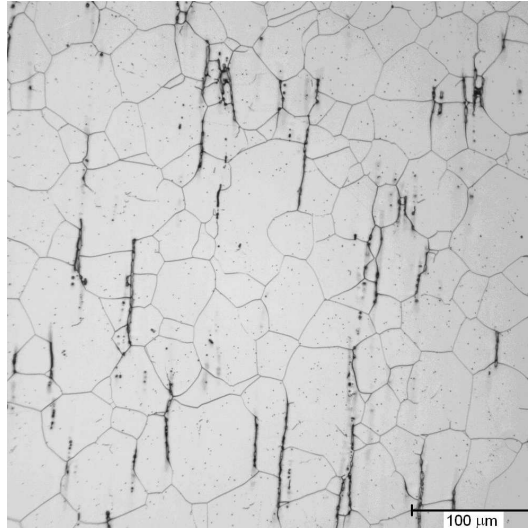


FIG. 3: Metallography of the 316L plate after annealing, taken normal to one of the rolling directions. The scale bar is 100 μm long.

the annealed plate and was instrumented with two strain gages type CEA-09-032UW-120, aligned along the rolling x -direction on the bottom surface. The cut was executed starting from the opposite surface (top) in 0.38 mm increments to a depth of 12.57 mm, using a wire electric discharge machine (EDM) with a 250 μm brass wire. The original residual stress were determined from the measured strains using the regularized pulse method¹⁵. The resulting stress magnitudes were lower than 10 MPa, confirming the effectiveness of the annealing process.

After annealing, a metallographic analysis was made on the plate to check the grain-size (see Fig. 3), whose average is about 50-100 μm , with some smaller grains. The metallography also revealed the presence of about 0.5% of ferrite, seen as dark stringers, which is not enough to cause any multi-phase problems with the neutron diffraction measurements of residual strains. A small amount of ferrite is typical in 316L stainless.

Constitutive data was required in order to model the material response during the indentation process. For this reason several compression tests, in accord with ASTM standard, were carried out in order to test the mechanical behavior of the material in the through-thickness direction and in the two in-plane directions. Cylindrical specimens, 9.5 mm in diameter and 12.7 mm height, were extracted from the plate. Displacement-control compression tests with a crosshead speed of 0.046 mm/min were executed until $\sim 20\%$ of engineering strain and then unloaded. The displacement was measured using a compression extensometer with

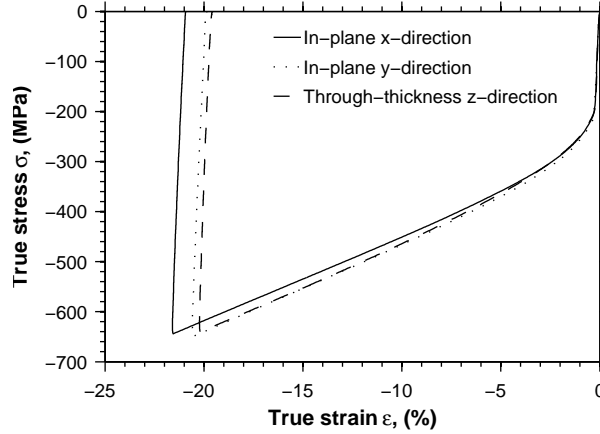


FIG. 4: True stress - true strain curves of uniaxial compression tests for the 316L stainless steel along the three material directions.

its arms mounted between the platens. The rate was chosen to give approximately the same strain rate as the one expected during the specimen indentation ($\dot{\epsilon} = 5 \cdot 10^{-5} \text{ sec}^{-1}$ after correcting for machine compliance). Figure 4 shows the true stress - true strain curves for the three tested material directions. The three curves are very close until the strain exceeds 5%. Considering that except for very localized regions at the indenter edge, the plastic strains from indentation are less than 2%, the material is taken as behaving isotropically. From the slope of the linear part (unloading) of these curves the Young's modulus, E , was found to be 193 GPa while the yield stress S_y is 208 MPa (0.2% offset yield strength). The linear part of the curve during loading gave a Young's modulus lower than the expected value for this steel. However, after few consecutive load-unload cycles in the elastic range, the linear loading curve rose to the expected value. Probably, the annealing process resulted in some plasticity at very low loads.

Although not originally planned, cyclic stress-strain curves were also measured in order to accurately model the specimens. Preliminary FE simulation of the indentation process showed that the predicted residual stress field is affected, besides by the plastic behavior during loading, also by the hardening model for unloading. In fact, the 316L stainless steel exhibits a strong Bauschinger effect^{16,17}, and, furthermore, the indentation process produces some reverse loading in the central region. So, in order to calibrate a hardening model for the FE simulation, cyclic compression and tension tests were performed. Two specimens were extracted from each in-plane material direction of the 316L stainless steel plate. The

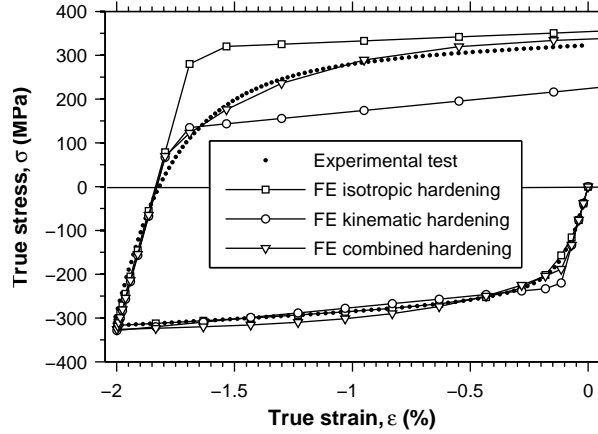


FIG. 5: Hardening behavior of the 316L in a uniaxial compression and tension together with the FE combined hardening model.

specimens were 69.85 mm long with a diameter of 5.08 mm and a gage length of 15.24 mm with threaded ends. Because of the small plate thickness, no cyclic specimens were made in the through-thickness direction. Since the preliminary FE simulations showed that the maximum equivalent plastic strain in the central region of the disk under the indenters was approximately of 2%, symmetric controlled strain cyclic tests were executed with a strain range, $\Delta\varepsilon$, of 4% (i.e. maximum strain of 2%). A strain rate of $4.5 \times 10^{-5} \text{ sec}^{-1}$ was used, which is the same as that which occurs in the majority of the disk during the indentation. The true stress - true strain curve of one cyclic test is shown in Fig. 5 together with the FE isotropic, kinematic and combined hardening model that were calibrated on this test and described in section V. There was no significant difference in the cyclic test in the other in-plane direction.

IV. INDENTATION TESTS

Several disks of 316L stainless steel were indented in the same experimental conditions in order to get virtually the same residual stress field. An Instron 1125 testing machine was used, and the displacement of the punch of the machine were measured with a Keyence magnetic sensor. The specimens were indented to a peak load of 90 kN under displacement control using a crosshead speed of 0.15 mm/min. A MOLYCOTE[®] anti-friction coating was applied on the contact surfaces of the two indenters. The relative alignment of the indenters

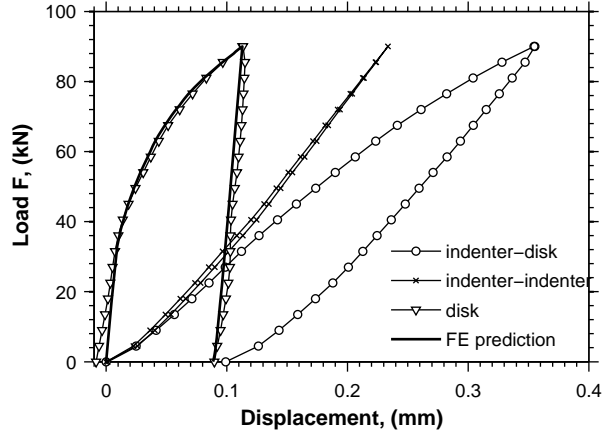


FIG. 6: Load - displacement curves of the indentation process of the 316L SS disk and its FE prediction.

respect to the rolling directions of the 316L was kept the same for the indentations of all the specimens. After the test, a footprint in both sides of the disk was produced with a thickness reduction of -0.85%.

Since the displacement measurement (circle-line in Fig. 6) is affected by the compliance of the specimen, the indenters, the lubricant and part of the test machine, due to the position of the displacement sensor, a preliminary test without any specimen (indenter versus indenter) was executed at the same maximum load to measure the in series compliance of the indenters-lubricant-test machine system (x-line in Fig. 6). By subtracting the measured displacements of the two tests, the displacements at the indenter-specimen interface were obtained (triangle-line in Fig. 6). The curves for the various indentations of different disks in the same experimental conditions varied by ± 0.005 mm. Figure 6 also shows the prediction of the load-displacement curve obtained with a FE simulation of the indentation process, which will be described in the next section.

V. MODELING

The residual stress field produced by the indentation was simulated using the ABAQUS[®] finite element code¹⁸. A half-symmetry axi-symmetric model of the specimen was built using 15,000 four-node quadrilateral elements (CAX4R) with reduced integration. Square elements 0.1 mm on a side gave a 50 x 300 mesh in the disk. The indenter was modeled using the same

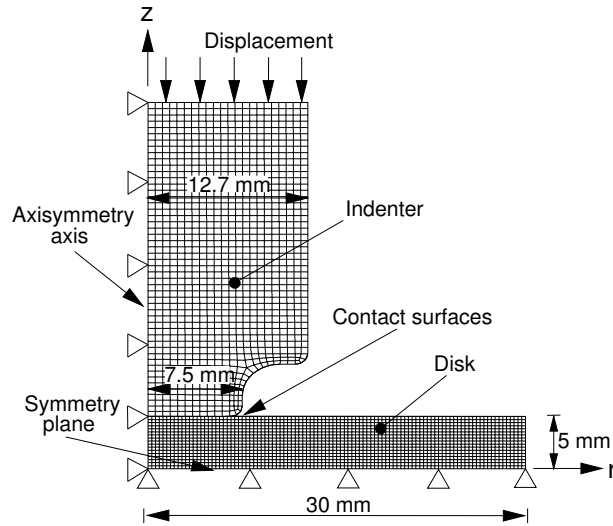


FIG. 7: Details of the axial-symmetric finite element model used showing the planes of symmetry.

element type but with a coarser mesh of 8,725 elements approximately 0.2 mm on a side. Figure 7 shows the FE model. The contact behavior between the indenter (master surface) and the disk (slave surface) was assumed frictionless because lubricant was used during the experimental test, and a surface-to-surface contact algorithm was used. Axi-symmetric boundary conditions were imposed along the axis of the indenter and the specimen, while symmetric boundary conditions were imposed on the middle plane of the specimen. A displacement of -0.09 mm in the z -direction was applied at the upper face of the indenter (the actual cross-head displacement is the double due to the symmetry) in order to achieve the experimentally applied load of -90 kN.

Initial model comparisons with measured residual stresses revealed that a more accurate material hardening model was needed in order to obtain satisfactory agreement. The behavior of 316L stainless steel was initially modeled using an isotropic and a kinematic hardening model, both calibrated on the compression-only experimental data. The indentation load-displacement, like Fig. 6, curves obtained from the FE analysis for both isotropic and kinematic hardening do not exhibit any noticeable difference, except a little difference during the unload for less than 10 kN. However, both models gave a poor prediction of the stresses in the indented disk when compared to experiments. These models were then calibrated on the cyclic data by running FE analysis on a simple one element model, subjected to a uniaxial compression of -2% of true strain in the first step, followed by a tensile strain of 2% in the second step. As response, the isotropic hardening predicted higher tensile stress

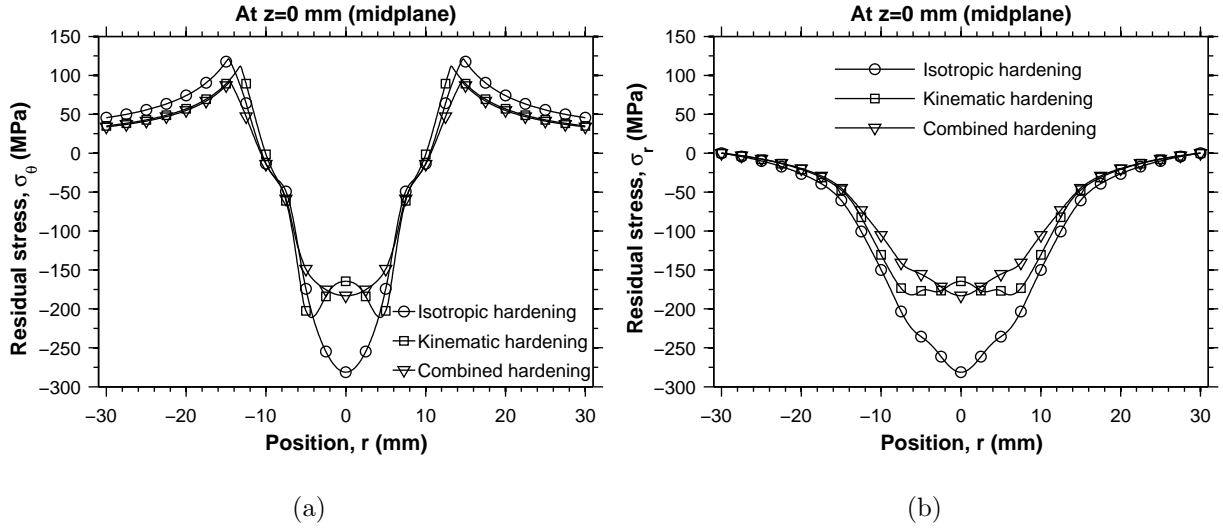


FIG. 8: Finite element model prediction of (a) hoop and (b) radial residual stresses along the mid-thickness line using isotropic, kinematic and combined hardening models of the 316L stainless steel.

than the experimental data after reverse loading (see Fig. 5), while the kinematic model gave lower stress. The predicted residual stress obtained using these two hardening models are showed in Fig. 8. It is evident that the different hardening model affects the residual stress because of reverse loading.

Since the experimental data from the cyclic test are in between the isotropic and kinematic hardening models (see Fig. 5), a combined hardening model that involves a kinematic term and an isotropic one in its formulation was used. In detail, the combined hardening model provided by ABAQUS^{®19} was used. This hardening model is based on the work of Lemaitre and Chaboche¹⁶. The pressure independent yield surface is defined by

$$F = f(\boldsymbol{\sigma} - \boldsymbol{\alpha}) - \sigma^0 = 0 \quad (1)$$

where σ^0 is the size of yield surface and $f(\boldsymbol{\sigma} - \boldsymbol{\alpha})$ is the equivalent Mises stress with respect to the back-stress tensor $\boldsymbol{\alpha}$, that is defined by

$$f(\boldsymbol{\sigma} - \boldsymbol{\alpha}) = \sqrt{\frac{3}{2}(\mathbf{S} - \boldsymbol{\alpha}^{\text{dev}}) : (\mathbf{S} - \boldsymbol{\alpha}^{\text{dev}})} \quad (2)$$

where \mathbf{S} is the deviatoric stress tensor, $\boldsymbol{\alpha}^{\text{dev}}$ is the deviatoric part of the back-stress tensor and the symbol $:$ is the double contracted product.

The isotropic hardening behavior of the model defines the evolution of the yield surface size, σ^0 , as a function of the equivalent plastic strain, $\bar{\epsilon}^{pl}$

$$\sigma^0 = \sigma_0 + Q(1 - e^{-b\bar{\epsilon}^{pl}}) \quad (3)$$

where σ_0 is the yield stress at zero plastic strain, Q and b are material parameters. The non-linear kinematic hardening component is defined by an additive combination of a linear term and a relaxation term, which introduces the non-linearity:

$$\dot{\boldsymbol{\alpha}} = \frac{C}{\sigma^0}(\boldsymbol{\sigma} - \boldsymbol{\alpha})\dot{\bar{\epsilon}}^{pl} - \gamma\boldsymbol{\alpha}\dot{\bar{\epsilon}}^{pl} \quad (4)$$

The parameters for this combined hardening model were calibrated from the cyclic test described before using the procedure described in¹⁸ and their values are: $\sigma_0 = 185$ MPa, $C = 28722$ MPa, $\gamma = 230.7$, $Q = 100$ MPa and $b = 12$.

The indenter material (A2 tool steel) was modeled by assuming linear elastic behavior, since the stresses do not approach yield, which is more than 1300 MPa, during indentation.

The load-displacement curve obtained from the FE analysis considering the combined hardening model is shown in Fig. 6. Figure 7 shows the comparison of the FE prediction of the hoop and radial stress due to indentation using the isotropic, kinematic and combined hardening model respectively. The stresses under the indenter are quite sensitive to the hardening model because of significant reverse plasticity.

Figure 9 shows the contour maps of the radial, hoop and axial residual stress modeled using the combined hardening model that better simulates the 316L stainless steel. Fig. 9(c) also shows the region where the reverse plasticity is more than 0.001 (0.1%)(cross hatched region).

VI. NEUTRON DIFFRACTION EXPERIMENT

Stress maps were measured using the SMARTS instrument at the Los Alamos Neutron Science Center (LANSCE). LANSCE is a pulsed neutron source where each pulse contains a spectrum of wavelengths and is moderated by passing through a chilled water moderator at 10 °C. The incident flight path on SMARTS is 31 m, most of it in a neutron guide. SMARTS has two detector banks at plus and minus 90 degrees to the incident beam with a diffracted flight path length of about 1.5 m, see Fig. 10(a). The total flight path, the

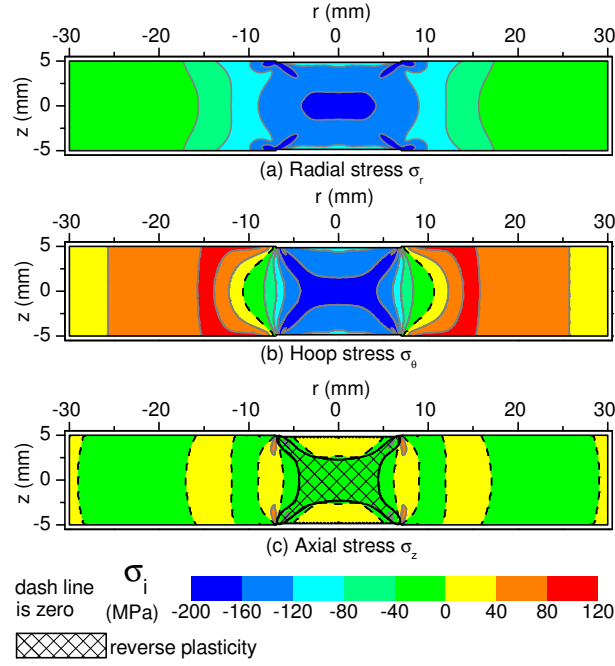


FIG. 9: Finite element model of the radial, hoop and axial residual stresses along the diameter plane using the ABAQUS combined hardening model of the 316L stainless steel. The cross hatched region in (c) is where reverse plasticity occurs.

scattering geometry and the 20 Hz repetition rate of the source dictates that the useable wavelength range on SMARTS is about 0.4 to 3.8 Å with maximum intensity between 0.5 to 1.5 Å.

Strains were measured along the three principal directions at 123 gage volumes which locations are shown in Fig. 11, spaced by 1.7 mm from each other in the central part (for $-15.3 \text{ mm} \leq r \leq 15.3 \text{ mm}$) in order to better follow the high strain gradient in the central region of the disk and 3.4 mm elsewhere. Because of limited experimental time, Fig. 11 reflects that the full intended grid was not measured in all quadrants of the cross-section. The incident slits were set to $2 \times 2 \text{ mm}^2$, and a set of radial collimators limited the gauge volume to 2 mm along the incident beam path. The disk was positioned so that the scattering vector for the +90 degrees bank, Q_1 , was along the axial (z) direction, and the scattering vector for the -90 degrees bank, Q_2 , was along the radial (r) direction of the disk. A series of measurements were made on a cross-section through the center. Then the disk was rotated 90 degrees around the axial z direction, and another scan was performed in the vertical direction (out of the plane of the paper in Fig. 10(a)). The first and second scans were made in the same

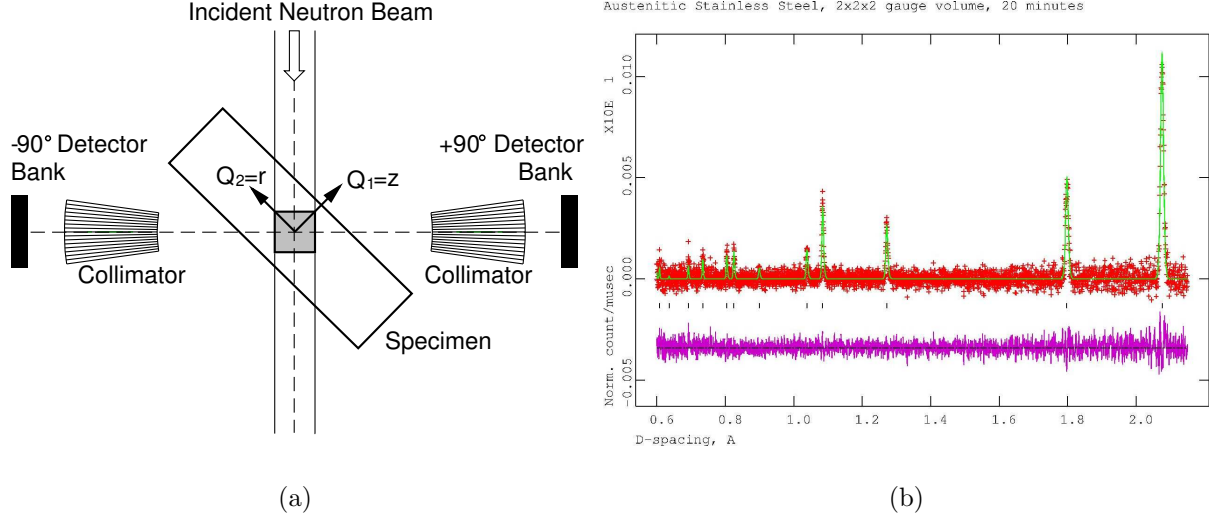


FIG. 10: (a) Schematic setup of SMARTS for spatially resolved measurements, and (b) Typical diffraction pattern. The red crosses are the data, the green line is the Rietveld refinement and the magenta line is the difference curve. The black tick-marks indicate the positions of the face-centered cubic peaks.

physical positions within the disk, but in the first scan the radial strains, ε_r , were measured in the -90 degrees bank, and in the second scan the hoop strains, ε_θ , were measured in the -90 degrees detector bank. In both scans the axial strains, ε_z , were measured in the +90 degrees bank. Further measurements were also executed on an un-indented, annealed disk (disk C).

A typical diffraction pattern for the 316L stainless steel from this study is shown in Fig. 10(b). Many peaks from the austenitic stainless steel are present enabling Rietveld full pattern analysis²⁰. Being able to use multiple peaks in the refinement greatly improves the statistics, and using the GSAS software²¹ we can determine the lattice parameter, a , of the *fcc* crystal structure with a relative accuracy of about 50×10^{-6} , or 50 microstrain ($\mu\varepsilon$), using count times on the order of 20 minutes for the 8 mm^3 sampling volumes.

The lattice strains are calculated based upon a stress-free reference measurement. In this case the average stress-free lattice parameters from a series of measurements on three small cubes ($5 \text{ mm} \times 5 \text{ mm} \times 5 \text{ mm}$) were determined. Then the residual strains can be calculated as follows:

$$\varepsilon_i = \frac{a_i}{a_i^0} - 1 \quad i = r, \theta, z \quad (5)$$

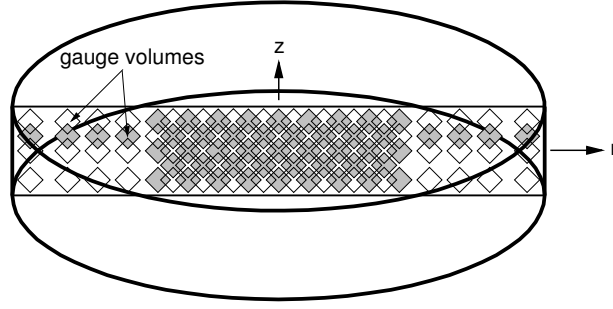


FIG. 11: Location of gauge volumes (2 mm x 2 mm x 2 mm) for the neutron measurements. Some gauge volumes are colored gray in order to distinguish overlapping volumes.

where a_i and a_i^0 are the stresses and unstressed lattice parameters, respectively, in the test specimen and in the stress-free cubes along the different directions (r , θ and z). Then the residual stress components were evaluated using Hooke's law:

$$\sigma_i = \frac{E(1-\nu)}{(1+\nu)(1-2\nu)} \left[\varepsilon_i + \frac{\nu}{1+\nu} (\varepsilon_j + \varepsilon_k) \right] \quad i, j, k = r, \theta, z \quad (6)$$

where E is the elastic modulus, and ν is Poisson's ratio.

VII. CONTOUR METHOD

The residual hoop stresses on a diametrical plane of two disks (disk A and B) indented under the same experimental conditions were measured with the contour method. Disk A was the same scanned by neutron diffraction and was cut in half along the scanned plane using wire EDM and a 50 μm diameter tungsten wire. Because of errors attributed to the thin wire, disk B was cut using a 100 μm diameter brass wire. Both disks were submerged in temperature-controlled deionized water throughout the cutting process. "Skim cut" settings were used. The disks were constrained by clamping on both sides of the cut to the work plate of the EDM machine. To prevent any thermal stresses, the specimens and the fixture were allowed to come to thermal equilibrium in the water tank before clamping. The clamping direction was parallel to the wire axis. As controls, two unindented disks were cut using the 50 μm and 100 μm diameter wire respectively.

After cutting, disk A was removed from the clamping fixture. The contours of both cut surfaces were measured using a Taylor-Hobson Talyscan 250 laser scanner. A laser triangulation probe of 2 mm range and resolution of 0.1 μm was used. The cut surfaces

were measured on a 0.1 mm spaced grid, giving about 60,000 points on each cut surface. The measured shapes are not plotted here because of space limitations but are available elsewhere²². The peak-to-valley amplitude of the contour is about 40 μm . The primary shape of the contour is high in the center of the disk and lower at the diameter edges. Disk B was measured using the laser scan machine described before²³. The surfaces were scanned using rows separated by 0.1 mm in the axial direction, z , with data points within a row sampled every 0.04 mm, giving about 113,000 points on each cut surface.

The cut surfaces of the two unindented disks were also measured using the two laser scan machines mentioned above. The contour of the unindented disk that was cut using the 100 μm brass wire was flat to within measurement resolution. The contour of the unindented disk that was cut using the 50 μm tungsten wire was higher by about 6 μm on the top and bottom edges of the 10 mm thickness than in the mid-thickness. Recall that slitting test on the annealed 316L material indicated that the post-annealing stresses were less than 10 MPa. Therefore, this contour is probably caused by the EDM cutting and not by residual stress since it would require stresses over 100 MPa to produce such a contour. In fact, the wire used had half the diameter of the smallest wire previously reported for contour measurements. So, in order to correct this effect the contour on the unindented disk was subtracted from the contour of the indented disk A, which was cut with the same wire.

The hoop stresses that were originally present on the plane of the cut of each disk were calculated numerically by elastically deforming the cut surface into the opposite shape of the contour that was measured on the same surface²⁴. This was accomplished using a 3-D elastic finite element (FE) model. A model was constructed of one half of the disk. The mesh used 51,920 linear hexahedral 8-node elements with reduced integration (C3D8R). The material behavior was considered elastically isotropic with an elastic modulus of 193 GPa and a Poisson's ratio of 0.3. The raw data was processed into a form suitable to calculate stresses using a procedure described in detail elsewhere²³. The data from each half was interpolated onto a common grid and then averaged to remove several potential error sources. In order to smooth out noise in the measured surface data and to enable evaluation at arbitrary locations, the data were fitted to a bivariate smoothing spline. The smoothing spline fits were evaluated at a grid corresponding to the FE nodes, and those values at the nodal locations were then used as displacement boundary conditions in the direction normal to the cut surface.

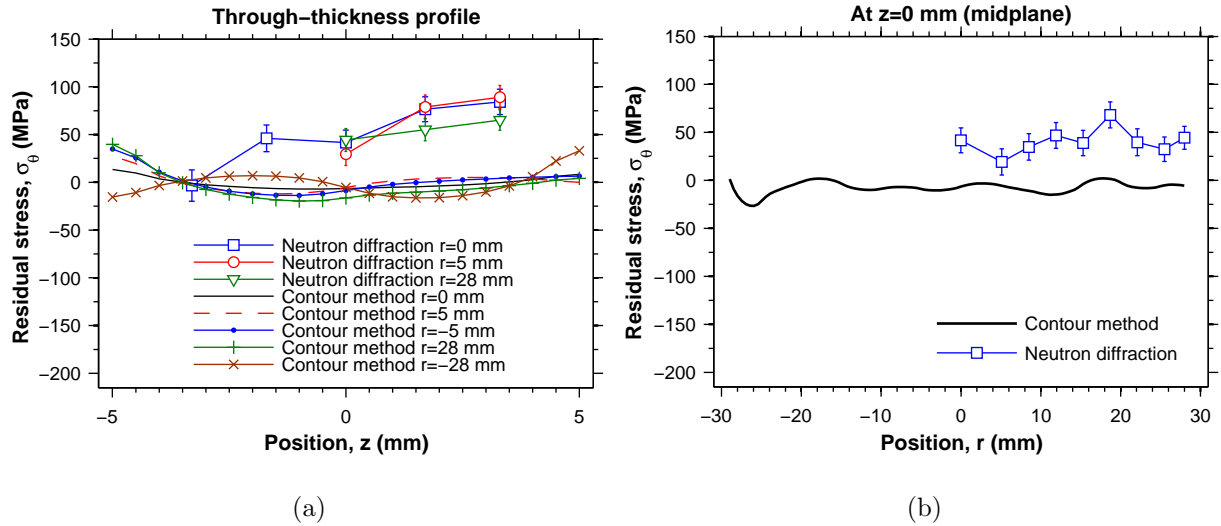


FIG. 12: Residual stress measured with the contour method and neutron diffraction on unindented disks of the stress-relieved 316L steel.

VIII. RESULTS AND DISCUSSION

The stress measurements on the unindented disks of the stress-relieved 316L steel, which had been independently measured to have stress magnitudes below 10 MPa, indicate resolution limits for the measurement methods. In Fig. 12, the contour results from the test cut with 100 μm diameter wire are plotted at the locations of the neutron measurements for comparison purposes. The contour results are generally less than ± 20 MPa except at isolated regions near the edges. The contour results on the disk cut with the 50 μm diameter wire are not plotted but exceed 100 MPa, illustrating the importance of testing before using unproven cutting conditions. The neutron results average over 40 MPa in tension with the unstressed lattice parameters that were determined carefully from measurements on three small cubes taken from the stress-relieved plate. Subsequent neutron results were not corrected to choose a more favorable value for unstressed lattice spacing because that would be an a posteriori adjustment based on assumed knowledge about the results.

The experimental measurements on the indented disks agree with each other and the FE model within the experimental resolution limits, indicating the suitability of these validation specimens. Figures 13 and 14 show stress maps measured by neutron diffraction and the contour method, respectively, for comparison with the FE-model stress maps of Fig. 9. Figures 15 and 16 show line plots extracted from the stress maps. The FEM results are point wise stress values. Based on the stress gradients, the effects of averaging over the

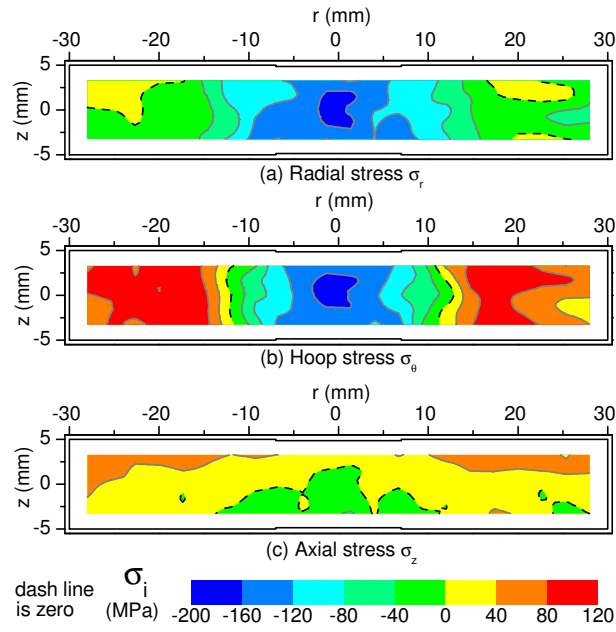


FIG. 13: Maps of (a) radial, (b) hoop and (c) axial residual stresses measured with neutron diffraction on the diametrical plane.

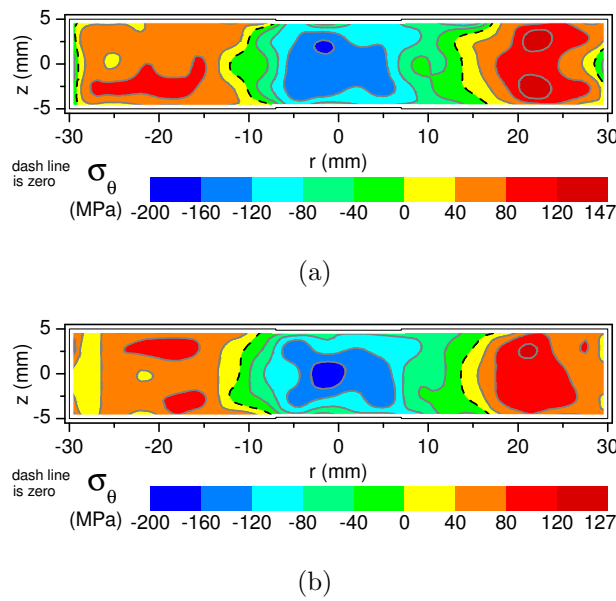


FIG. 14: Residual hoop stress map measured with the contour method along the diameter plane for (a) the disk A and (b) disk B.

sampling volume is estimated to be less than ± 5 MPa. The overall agreement is quite good. The most obvious discrepancies appear in the low magnitude axial stresses where apparent errors in unstressed lattice spacing shift the entire profile.

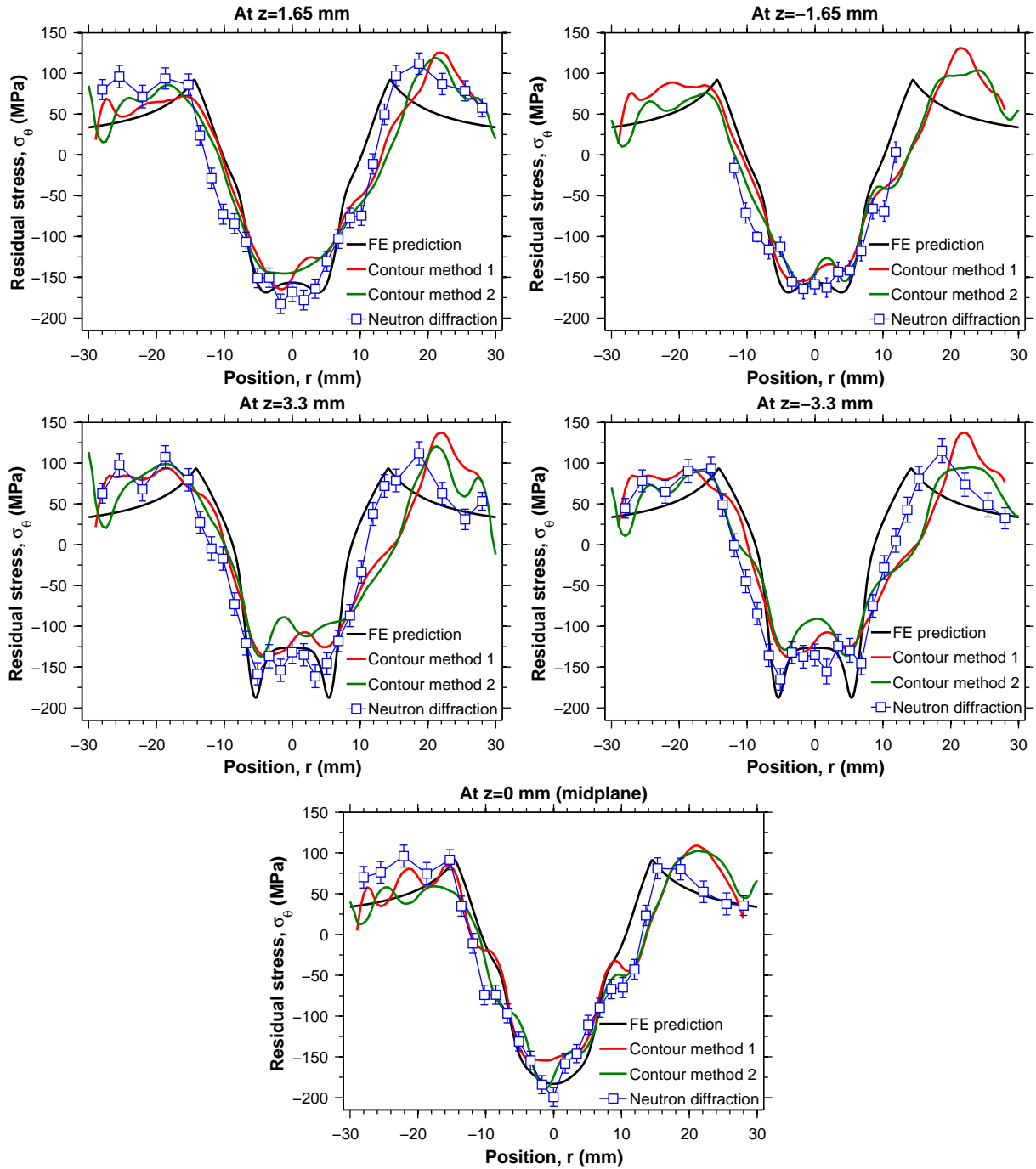


FIG. 15: Hoop residual stresses measured with neutron diffraction and contour method compared to the FE model.

Root mean square averages of the differences between hoop stress values from Fig. 15 were calculated and are given in Table I. To better interpret the results for possible measurement on other materials, values are also given in microstrain because strain or deformation is a better measure of the sensitivity of the measurement methods. The best agreement is

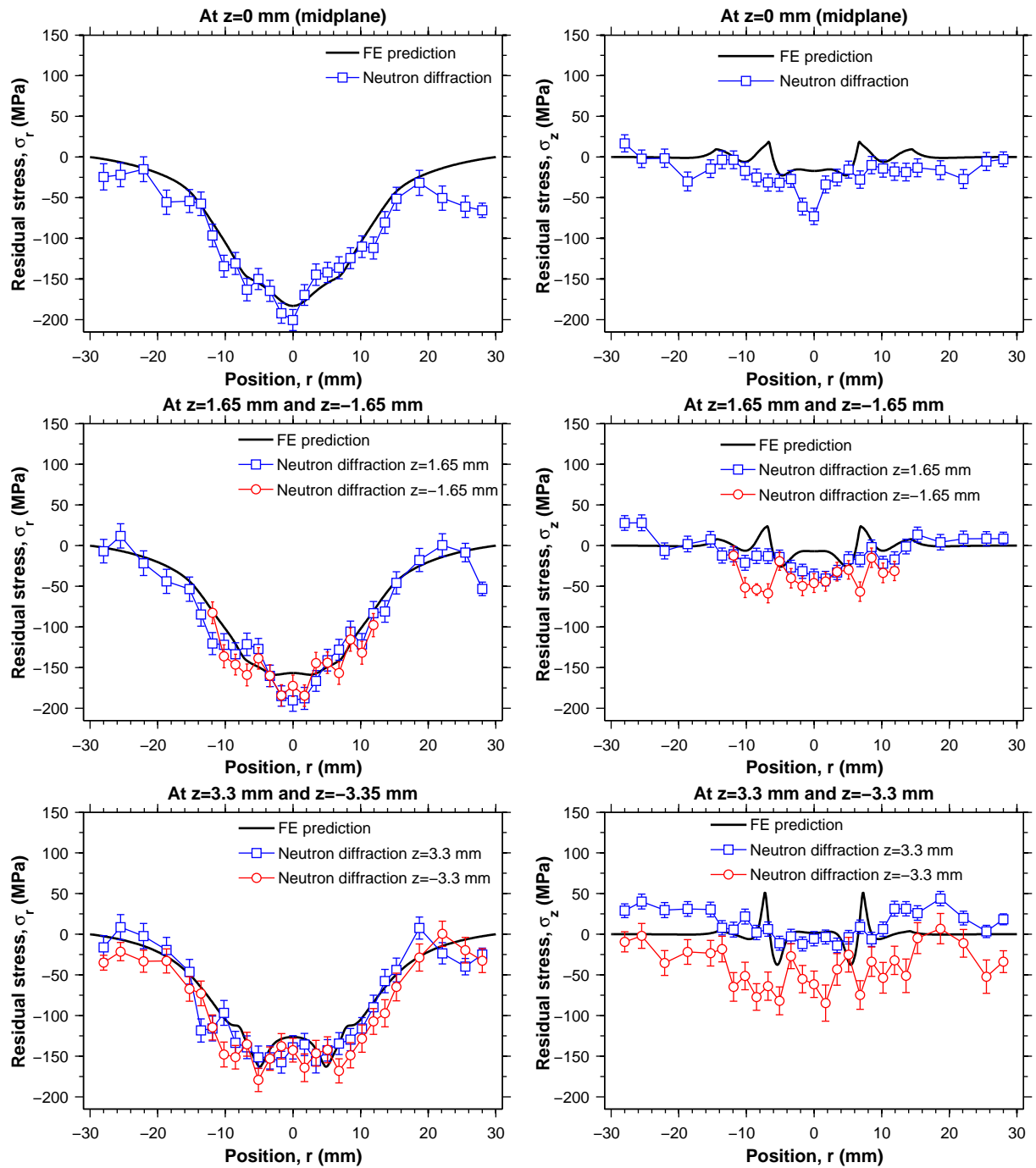


FIG. 16: Radial and axial residual stresses measured with neutron diffraction compared to the FE model.

between the two contour measurements at about 20 MPa or $100 \mu\epsilon$ which is excellent repeatability. The neutron diffraction agrees with both contour measurements to about 28 MPa or $145 \mu\epsilon$, which is also excellent agreement especially considering the results in the unindented disks. The finite element model agrees with all three of the measurements

TABLE I: Root-mean-square difference between pairs of hoop stress measurements or the finite element model, over the neutron diffraction measurement locations.

MPa ($\mu\epsilon$)	Contour 2	Neutron	FE Model
Contour 1	20 (104)	27 (140)	32 (166)
Contour 2	–	28 (145)	33 (171)
Neutron	–	–	33 (171)

within about 33 MPa or 170 $\mu\epsilon$, which is still very good agreement when comparing with a model. Neither experimental method resolves some of the finer feature of the FE prediction, such as the X-shaped peak compressive stress region for the hoop stress. Therefore, such detail in the FE model cannot be considered to be experimentally validated.

Modeling the material hardening under reverse loading conditions appears to be the limiting factor in the fidelity of the FE model, and it could be improved. Figure 8 showed the sensitivity of the modeled residual stresses to the hardening model. The hardening model was calibrated using data only from symmetric strain-controlled cyclic experiments with a strain range $\Delta\epsilon$ of 4% (2% of true strain in compression followed by a 2% of true strain in tension). More calibration data with different strain amplitudes could improve the model since local regions of the disks sees up to 5% plastic strain and other regions see less than 2%. Other modeling assumptions likely have less effect. Changing the friction coefficient from 0.0 to 0.2 changed the stresses by less than 25 MPa at the measurement locations plotted in Fig. 15. The maximum heating from plastic work was estimated by a conservative, adiabatic FE analysis to be 5 K, which would only be expected to lower the yield stress by about 0.1% based on the temperature dependence of the shear modulus²⁵.

Some experimental conditions also affected the accuracy of the predictions. The measurement of the indentation footprint indicated that the thickness reduction may have differed from perfect axisymmetry by about 4%. The resulting effect on stresses is not easily estimated. The asymmetry may have occurred because of imperfect colinearity of the two indenters. A tighter parallel tolerance on the indentation surface relative to the opposite surface of the indenter (the one loaded by the machine) might improve that colinearity. However, a more error tolerant design, such as a radiused rather than flat indenter surface, would probably be more productive.

The type of EDM wire used probably led to the need to correct the contour of disk A based on the contour of a cut in a stress-free disk. This demonstrates the importance of always making a control cut in a stress free material. The wire used on disk A was, at 50 μm , half the diameter of the one used on disk B and it was also tungsten as compared to brass. There is not sufficient information to tell which difference caused the cut to be non-flat even in a stress-free disk. The only previous time such a correction was necessary in the authors' experience was for a 100 μm brass wire that was unusual in that it was zinc-coated²⁴. However, we note that other unpublished measurements using the small tungsten wire have been quite successful. The use of a small wire can be advantageous because some error sources are reduced with a thinner cut.

Comparing the two contour method measurements demonstrates not only repeatability of the method but also has important implications for more complicated parts. The rms difference between the two contour results of 20 MPa or 0.01% of E would be quite good and comparable to other methods if the measurements had been performed under identical experimental conditions. Since the cut on disk A used a different EDM wire and required a correction of up to 50 MPa based on the cut made on stress-free disk, the agreement is more impressive. For this specimen, the correction could have been avoided by better choice of the cutting wire based on stress-free testing. However, in parts with a more complicated cross-section, such errors may be present no matter the cutting conditions because the width of the EDM cut will change slightly as the thickness of the part changes during the cut. Based on the results of the measurements on the two disks, a correction based on a cut in a stress-free part could successfully correct for such errors.

Acknowledgments

Much of this work was performed at Los Alamos National Laboratory, operated by the Los Alamos National Security, LLC for the National Nuclear Security Administration of the U.S. Department of Energy under contract DE-AC52-06NA25396. This work has benefited from the use of the Lujan Neutron Scattering Center at Los Alamos Neutron Science Center, which is funded by the Department of Energy's Office of Basic Energy Sciences. Mr. Pagliaro's work was sponsored by a fellowship from the Università degli Studi di Palermo. The authors would like to thank Professor Michael Hill at U.C. Davis for the scanning of the surface

contours.

-
- ¹ Withers, P. J., 2007, “Residual Stress and Its Role in Failure,” *Reports on Progress in Physics*, **70**(12), pp. 2211–2264.
 - ² Hill, M. R., DeWald, A. T., Rankin, J. E., and Lee, M. J., 2005, “Measurement of Laser Peening Residual Stresses,” *Materials Science and Technology*, **21**(1), pp. 3–9.
 - ³ Hatamleh, O., Lyons, J., and Forman, R., 2007, “Laser Peening and Shot Peening Effects on Fatigue Life and Surface Roughness of Friction Stir Welded 7075-T7351 Aluminum,” *Fatigue and Fracture of Engineering Material and Structures*, **30**(2), pp. 115–130.
 - ⁴ Woo, W., Choo, H., Prime, M. B., Feng, Z., and Clausen, B., 2008, “Microstructure, Texture and Residual Stress in a Friction-Stir-Processed Az31b Magnesium Alloy,” *Acta materialia*, **56**(8), pp. 1701–1711.
 - ⁵ Withers, P. J., Turski, M., Edwards, L., Bouchard, P. J., and Buttle, D. J., 2008, “Recent Advances in Residual Stress Measurement,” *International journal of pressure vessels and piping*, **85**(3), pp. 118–127.
 - ⁶ Martineau, R. L., Prime, M. B., and Duffey, T., 2004, “Penetration of HSLA-100 Steel with Tungsten Carbide Spheres at Striking Velocities between 0.8 and 2.5 km/s,” *International Journal of Impact Engineering*, **30**(5), pp. 505–520.
 - ⁷ Prime, M. B., Gnäupel-Herold, T., Baumann, J. A., Lederich, R. J., Bowden, D. M., and Sebring, R. J., 2006, “Residual Stress Measurements in a Thick, Dissimilar Aluminum Alloy Friction Stir Weld,” *Acta Materialia*, **54**(15), pp. 4013–4021.
 - ⁸ Kelleher, J., Prime, M. B., Buttle, D., Mummery, P. M., Webster, P. J., Shackleton, J., and Withers, P. J., 2003, “The Measurement of Residual Stress in Railway Rails by Diffraction and Other Methods,” *Journal of Neutron Research*, **11**(4), pp. 187–193.
 - ⁹ DeWald, A. T. and Hill, M. R., 2006, “Multi-Axial Contour Method for Mapping Residual Stresses in Continuously Processed Bodies,” *Experimental Mechanics*, **46**(4), pp. 473–490.
 - ¹⁰ Pagliaro, P., Prime, M. B., and Zuccarello, B., 2006, “Multi Stress Components From Multiple Cuts For the Contour Method,” *Proceedings of the XXXV AIAS Conference*, Università Politecnica delle Marche, Ancona, Italy.
 - ¹¹ Mahmoudi, A. H., Stefanescu, D., Hossain, S., Truman, C. E., Smith, D. J., and Withers, P. J.,

- 2006, “Measurement and Prediction of the Residual Stress Field Generated by Side-Punching,” *Journal of Engineering Materials and Technology*, **128**(4), pp. 451–459.
- ¹² Korsunsky, A. M., Liu, J., Golshan, M., Dini, D., Zhang, S. Y., and Vorster, W. J., 2006, “Measurement of Residual Elastic Strains in a Titanium Alloy Using High Energy Synchrotron X-ray Diffraction,” *Experimental Mechanics*, **46**(4), pp. 519–529.
- ¹³ Ezeilo, A. N. and Webster, G. A., 2000, “Neutron Diffraction Analysis of the Residual Stress Distribution in a Bent Bar,” *Journal of Strain Analysis for Engineering Design*, **35**(4), pp. 235–246.
- ¹⁴ Cheng, W. and Finnie, I., 2007, *Residual Stress Measurement and the Slitting Method*, Springer Science+Business Media, LLC, New York, NY, USA.
- ¹⁵ Schajer, G. S. and Prime, M. B., 2006, “Use of Inverse Solutions for Residual Stress Measurements,” *Journal of Engineering Materials and Technology*, **129**(3), pp. 375–382.
- ¹⁶ Lemaitre, J. and Chaboche, J.-L., 1990, *Mechanics of solid materials*, Cambridge University Press, Cambridge.
- ¹⁷ Choteau, M., Quaegebeur, P., and Degallaix, S., 2005, “Modelling of Bauschinger Effect by Various Constitutive Relations Derived from Thermodynamical Formulation,” *Mechanics of Materials*, **37**, pp. 1143–1152.
- ¹⁸ *ABAQUS User’s Manual, Version 6.6*, 2006, ABAQUS Inc., Pawtucket, RI.
- ¹⁹ *ABAQUS Theory Manual, Version 6.6*, 2006, ABAQUS Inc., Pawtucket, RI.
- ²⁰ Von Dreele, R. B., 1997, “Quantitative Texture Analysis by Rietveld Refinement,” *Journal of Applied Crystallography*, **30**, pp. 517–525.
- ²¹ Larson, A. C. and Von Dreele, R. B., 1986, “General Structure Analysis System (GSAS),” Tech. Rep. Los Alamos Report No. LA-UR-86-748, Los Alamos National Laboratory, Los Alamos, NM.
- ²² Pagliaro, P., 2008, “Mapping Multiple Residual Stress Components Using the Contour Method and Superposition,” Ph.D. thesis, Università degli Studi di Palermo, Palermo, Italy.
- ²³ Prime, M. B., Sebring, R. J., Edwards, J. M., Hughes, D. J., and Webster, P. J., 2004, “Laser Surface-Contouring and Spline Data-smoothing for Residual Stress Measurement,” *Experimental Mechanics*, **44**(2), pp. 176–184.
- ²⁴ Prime, M. B., 2001, “Cross-Sectional Mapping of Residual Stresses by Measuring the Surface Contour After a Cut,” *Journal of Engineering Materials and Technology*, **123**(2), pp. 162–168.

²⁵ Chen, S. R., 2007, Private Communication, Los Alamos National Laboratory.

List of Figure Captions

1. Schematic diagram illustrating (a) the indentation process, (b) the conceptual residual stress distribution obtained.
2. Quarter-symmetry drawing of the indentation fixture, dimensions in mm. R1=1 mm and R2=3 mm.
3. Metallography of the 316L plate after annealing, taken normal to one of the rolling directions. The scale bar is 100 μm long.
4. True stress - true strain curves of uniaxial compression tests for the 316L stainless steel along the three material directions.
5. Hardening behavior of the 316L in a uniaxial compression and tension together with the FE combined hardening model.
6. Load - displacement curves of the indentation process of the 316L SS disk and its FE prediction.
7. Details of the axial-symmetric finite element model used showing the planes of symmetry.
8. Finite element model prediction of (a) hoop and (b) radial residual stresses along the mid-thickness line using isotropic, kinematic and combined hardening models of the 316L stainless steel.
9. Finite element model prediction of the radial, hoop and axial residual stresses along the diameter plane using the ABAQUS combined hardening model of the 316L stainless steel. The cross hatched region in (c) is where the reverse plasticity is.
10. (a) Schematic setup of SMARTS for spatially resolved measurements, and (b) Typical diffraction pattern. The red crosses are the data, the green line is the Rietveld refinement and the magenta line is the difference curve. The black tick-marks indicate the positions of the face-centered cubic peaks.
11. Location of gauge volumes (2 mm x 2 mm x 2 mm) for the neutron measurements. Some gage volumes are colored gray in order to distinguish overlapping volumes.

12. Residual stress measured with the contour method and neutron diffraction on undented disks of the stress-relieved 316L steel.
13. Maps of (a) radial, (b) hoop and (c) axial residual stresses measured with neutron diffraction on the diametrical plane.
14. Residual hoop stress map measured with the contour method along the diameter plane for (a) the disk A and (b) disk B.
15. Hoop residual stresses measured with neutron diffraction and contour method compared to the FE prediction.
16. Radial and axial residual stresses measured with neutron diffraction compared to the FE prediction.

List of Table Captions

1. Root-mean-square difference between pairs of hoop stress measurements or the finite element model, over the neutron diffraction measurement locations.